NANO LETTERS

pubs.acs.org/NanoLett

Letter

Single-Layer Clathrane: A Potential Superconducting Two-Dimensional Hydrogenated Metal Borocarbide

Xiaoyu Wang,* Warren E. Pickett, Matthew N. Julian, Rohit P. Prasankumar, and Eva Zurek*

Cite This: *Nano Lett.* 2025, 25, 15081−15088

Read Online

ACCESS | Metrics & More | Article Recommendations | Supporting Information

ABSTRACT: We propose a new family of two-dimensional (2D) metal borocarbide clathrane superconductors derived from three-dimensional (3D) $MM'B_6C_6$ clathrates. First-principles calculations reveal that hydrogen passivation and surface metal decoration stabilize the $M_2M'B_8C_8H_8$ monolayers. These 2D systems exhibit tunable superconductivity governed by hole concentration, structural anisotropy, and electron−phonon coupling. We find that in-plane anisotropy competes with superconductivity, reducing T_c despite favorable doping. Biaxial strain mitigates this anisotropy, enhances Fermi surface nesting, and increases T_c by an average of 15.5 K. For example, the T_c of $Sr_3B_8C_8H_8$ is predicted to increase from 11.3 to 22.2 K with strain engineering. These findings identify 2D clathranes as promising, strain-tunable superconductors and highlight design principles for optimizing low-dimensional superconducting materials.

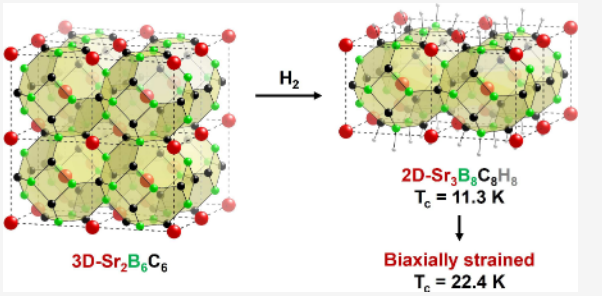

KEYWORDS: *borocarbides, superconductivity, chemical bonding, electronic structure, density functional theory, nanostructuring*

Nanostructuring, for example, by decreasing dimensionality, harnessing substrate-proximity effects, or using strain engineering, can influence a material's superconducting properties.[1−3] Nearly a century ago, the first studies on how dimensionality reduction affects superconductivity were performed on Pb and Sn.[4] Now, highly crystalline two-dimensional (2D) systems can be investigated.[5] The first demonstration of superconductivity in the ultimate 2D limit of a single atomic layer yielded a critical temperature (T_c) of 1.8 K for Pb grown epitaxially on Si(111).[6] Beyond fundamental interest, 2D superconductors are attractive for device miniaturization, enabling applications in quantum information science, nanoscale circuitry, and gate-tunable superconducting devices.[7−9] The superconducting properties of various 2D systems, including alkali-metal-intercalated few-layer graphene,[10−12] $NbSe_2$,[13−16] 2H-NbS_2,[17] and $TiSe_2$,[18] have been reported. The measured T_c values are sensitive to the nature of the intercalant and competition between the superconductivity and charge density waves (CDWs), layer thickness, and external electric fields. Density functional theory (DFT) studies predicted that the T_c of bulk LiC_6 increases from 0.9 to 8 K in the monolayer,[19] yielding a T_c of 18 K for monolayer Li_2C_6.[20] The influence of the layer thickness and magnetic and CDW order on the superconducting properties of $NbSe_2$ were investigated.[21,22] Strain-tunable 2D superconductors were predicted, including monolayer W_2N_3[23] and Janus monolayers of MoSH,[24,25] WSeH, and WSH.[26,27]

Boron-based compounds have also attracted considerable interest. While bulk MgB_2 exhibits a T_c of ∼40 K,[28] the T_c of a monolayer was predicted to be ∼20 K, which could be enhanced to over 50 K under biaxial strain[29] and further increased to 67 K via hydrogenation and even 100 K with additional strain engineering.[30] Other theoretically studied boron-rich systems include monolayers of B_2C,[31] B_2O,[32] TiB_3C, $Ti_2B_3C_2$,[33] and LiBC.[34] Boron-side hydrogenation of LiBC was predicted to increase T_c from 70 to 80 K,[34] while a TiB_3CH_2 monolayer was computed to have a T_c of 18.7 K.[33] A high-throughput study reported a T_c of 22 K for $Mg_2B_4N_2$,[35] isostructural to the previously predicted $Mg_2B_4C_2$ (T_c ∼ 47 K[36]), and a DFT and machine-learning hybrid study screened over 140,000 2D compounds for superconductivity.[37] Although experiments have yet to verify these computations, the borophene allotrope of boron was synthesized,[38] with computed T_c values reaching as high as 10−20 K.[39] The reactivity of borophene with oxygen hinders such applications. However, recent experiments demonstrated that hydrogen passivation can significantly enhance borophene's stability,[40] and subsequent theoretical studies predicted an increase in T_c up to 29 K under uniaxial strain.[41]

Herein, the superconductivity in the 2D analogues of a new class of borocarbides is studied via DFT calculations. The compounds SrB_3C_3[42,43] and LaB_3C_3[44] have been synthesized

Received: August 14, 2025
Revised: September 19, 2025
Accepted: October 2, 2025
Published: October 6, 2025

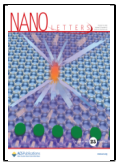

in bulk, with SrB_3C_3 exhibiting a T_c value of 22 K at 23 GPa.[42] Subsequent theoretical studies predicted additional superconducting phases including BaB_3C_3,[45] $RbSrB_6C_6$,[46] $Rb_{0.8}Sr_{1.2}B_6C_6$,[47] $KPbB_6C_6$,[48] $CsBaB_6C_6$,[49] $RbYbB_6C_6$,[50] $SrNH_4B_6C_6$, and $PbNH_4B_6C_6$[51] with T_c values as high as 115 K.[51] Anharmonicity was shown to effect the T_c value of $KPbB_6C_6$.[52] Structurally, $MM'B_6C_6$ clathrates resemble diamond: both are covalent solids built on sp^3 frameworks.[48] The synthesis conditions for compounds such as SrB_6C_6 (50−60 GPa and 2500 K)[42,43] closely resemble those required for diamond formation (typically >15 GPa and 1200 K).[53−55] However, while diamond has a 2D-layered counterpart known as diamane, which can be experimentally realized from bilayer graphene under pressure and/or surface passivation with hydrogen or fluorine,[56] the 2D analogue of $M_2B_6C_6$—a metal borocarbide "clathrane"—has not yet been explored. Below we investigate whether such a clathrane monolayer is theoretically viable and examine its superconducting properties.

Our model, illustrated in Figure 1A and B, features a single layer of the 3D clathrate with metal atoms positioned both at the center of the cage and on the surface within a half-cage configuration. Similar to diamane[57] and borophene,[40] surface passivation is essential for dynamic stability. Various termination schemes were evaluated—no passivation, bridge-site passivation with oxygen or sulfur, halogen termination, and hydrogenation—and only hydrogenation yielded local minima. The presence of surface metal atoms was also found to be critical for dynamic stability. By combining appropriate surface passivation and metal incorporation, we arrived at a stable composition with $M_2M'B_8C_8H_8$ stoichiometry, where M represents the surface metal and M′ denotes the encapsulated metal cation (Figure 1A). The choice of metals was guided by size compatibility with the B_6C_6 cage, including K, Rb, Ca, Sr, Ba, Y, La, Sn, and Pb, following previous theoretical results.[48]

Computations investigated the thermodynamic conditions required to stabilize the 3D clathrates,[43,48,49] and synthesized SrB_3C_3 was quenched to 1 atm, persisting in an inert atmosphere but degrading after exposure to moisture.[43] For the clathranes, the thermodynamic stability (at zero temperature and for static nuclei) was assessed by calculating the exfoliation energy (ΔE_{EXF}) defined as the energy of the products minus the reactants for the reaction:

$$2MM'B_6C_{6(s,3D)} + 4H_{2(g)} \rightarrow M_2M'B_8C_8H_{8(s,2D)} + M'_{(s)} + 4B_{(s)} + 4C_{(s)}$$

where B, C, and M′ correspond to the 1 atm stable phases of α-boron, graphite, and solid elemental metals in the face-centered-cubic (K, Ca, Pb), body-centered-cubic (Rb, Ba), hexagonal-close-packed (Sr, Y, La), or α-Sn structure, and H_2 is modeled by the $P6_3/m$ phase of solid molecular hydrogen.[58] The functional used underestimates the energy of graphite. Inclusion of dispersion corrections and consideration of further reactions is likely to stabilize the products (Section S4.1, S4.2). In many cases, with exceptions, such as Sn and Pb, the formation of a binary metal boride or metal carbide would strongly favor the forward reaction (Table S3). Therefore, the energy estimates presented here represent a lower bound for the thermodynamic driving force favoring hydrogenated 2D slab formation following exfoliation of the 3D crystal in a hydrogen atmosphere (Figure S4).

In most cases, the aforementioned process is exothermic (Figure 1C). Exceptions, highlighted in green, involve lanthanum, yttrium, and calcium atoms, where ΔE_{EXF} was predicted to range from 5.2 to 48.0 meV/atom. The reason for this is likely the enhanced stability of $MM'B_6C_6$ compounds that contain trivalent metal atoms because they are insulators. Notably, ΔE_{EXF} for the formation of $Sr_3B_8C_8H_8$ from $Sr_2B_6C_6$ was −72.3 meV/atom (−132.8 meV/atom with dispersion). The tendency for the formation of SrB_6 and SrC_2 on the product side further suggests that the forward reaction would be favored. A similar stabilizing effect has been established in diamane.[56] Without surface passivation, diamond nanosheets are unstable and reconstruct into multilayer graphene.[59] The strong C−H bonds ensure that diamane is resistant to dissociation, with activation barriers reaching up to 6 eV.[60] Our molecular dynamics simulations showed that $Sr_3B_8C_8H_8$ remains intact up to at least 500 K with a simulation length of 10 ps (Figures S2 and S3). Above 600 K, we observed dissociation of the B_2C_2 squares and reorganization into 5- or 6-membered rings. These results suggest that SrB_3C_3, which is thermodynamically unstable at 1 atm and reactive with air, may, upon hydrogenation, resist decomposition due to the strong B−H and C−H bonds formed within $Sr_3B_8C_8H_8$.

Bulk $MM'B_6C_6$ can be interpreted as a hole-doped compound relative to the ideal sodalite-type C_6 cage; the number of unoccupied C/B 2p states (i.e., holes) was found to correlate with dynamic stability.[46] For example, in $(Rb,Sr)_2B_6C_6$, imaginary phonons emerge when the rubidium concentration exceeds 50%,[46] and no dynamically stable clathrates were found when both M and M′ were alkali metals.[48−50] For the 2D clathranes, no dynamically stable structure was identified, with the number of holes (Table S2) exceeding 4 per formula unit (Figure 1C), further underscoring the necessity of both surface passivation and the inclusion of surface metal atoms. Previous studies reported a correlation between the dynamic stability and the ionic radius mismatch between the two guest metal species in the 3D clathrates[48]—an effect that also manifests in the 2D analogues. Interestingly, several structures fulfilling the requirement of less than 4 holes can also exhibit a single imaginary phonon mode at the X point

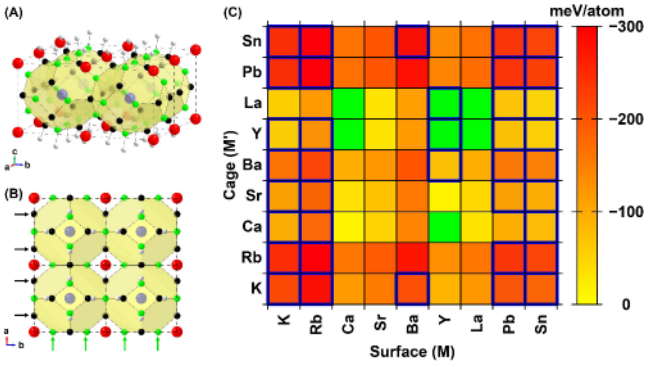

Figure 1. (A) Supercell of the 2D hydrogenated metal borocarbides ($M_2M'B_8C_8H_8$). Surface metals are red, cage metals are gray, boron is green, carbon is black, and hydrogen is white. (B) Top view of the structure. The equatorial boron/carbon atoms are marked with green/black arrows. (C) Energy (ΔE_{EXF}) associated with the formation of 2D structures along with solid M′, α-boron, and graphite via hydrogenation of the 3D structure. The green color shows regions where 3D structures are thermodynamically preferred (Ca_2Y, Ca_2La, Y_2Ca, Y_3, Y_2La, La_2Y, and La_3); otherwise, the color is scaled to the energy difference. Dynamically unstable structures are enclosed with blue squares.

https://doi.org/10.1021/acs.nanolett.5c04166
Nano Lett. 2025, 25, 15081−15088

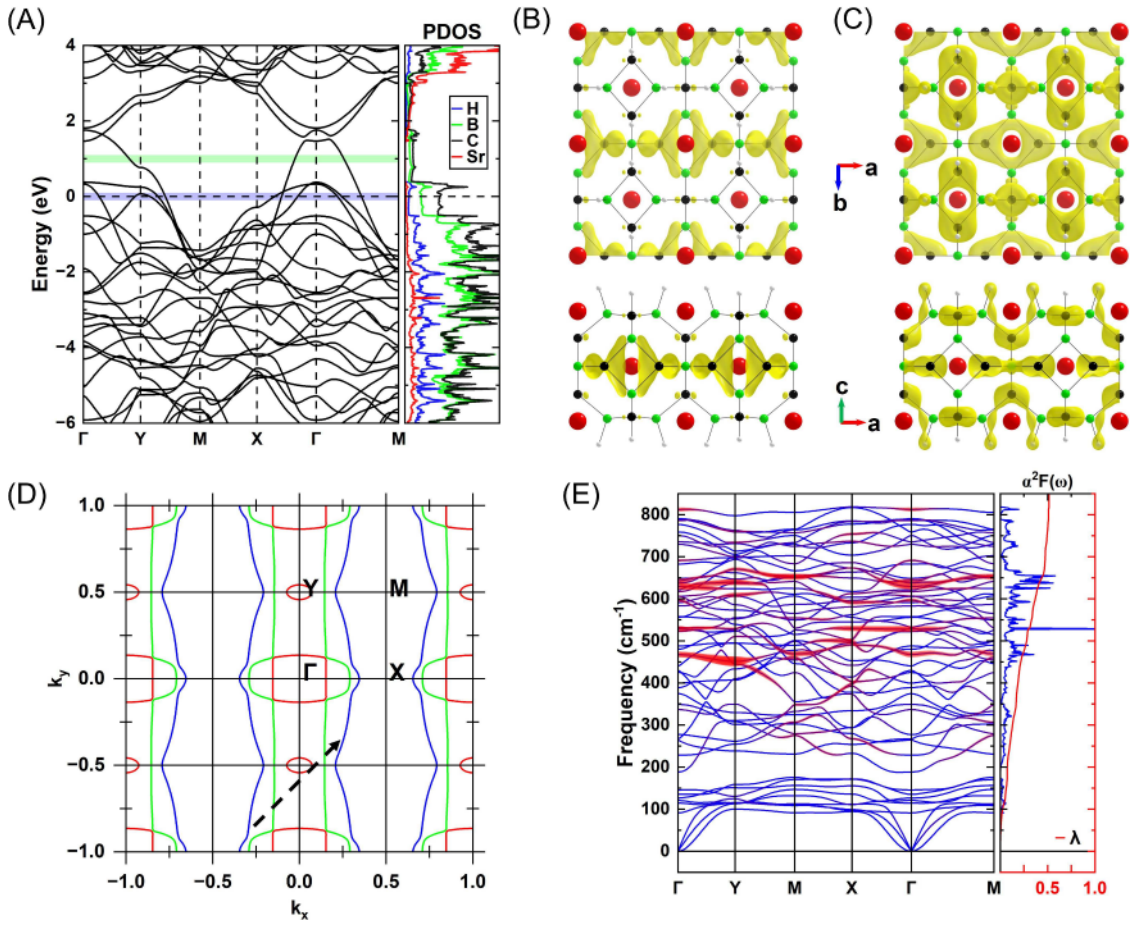

Figure 2. Electronic structure of $Sr_3B_8C_8H_8$. (A) Electronic band structure and atom projected density of states (PDOS) of $Sr_3B_8C_8H_8$. The Fermi level (E_F) is set to 0 eV. (B) Partial charge density integrated around E_F + 1 eV within an energy window of ±0.1 eV, corresponding to the green-shaded region in part A. (C) Partial charge density integrated around E_F within an energy window of ±0.1 eV, corresponding to the blue-shaded region in part A. The isosurfaces in parts B and C enclose 50% of the total charge within the selected energy windows. Atom color coding is consistent with Figure 1. (D) Fermi surface of the 2D $Sr_3B_8C_8H_8$ clathrane. The black dashed arrow illustrates an example of a **q** vector at the M point (q_x = 0.5 and q_y = 0.5) that connects nested electronic states on the steepest band. (E) Phonon dispersion, Eliashberg spectral function, $\alpha^2F(\omega)$, and the integrated electron−phonon coupling constant, $\lambda(\omega)$, within the frequency range of 0−800 cm^{-1}. The width of the red lines in the phonon dispersion corresponds to the mode-resolved electron−phonon coupling strength, proportional to $\lambda_{q\nu}\omega_{q\nu}$ for each phonon mode ν at wavevector **q**. The plot in the full frequency range is available in the Supporting Information.

[e.g., K_2Y (Figure S6H), Rb_2Y (Figure S7H), and Y_3 (Figure S13H)]. Visualization of these modes reveals a "super-dimerization" motion of neighboring cage-metal atoms, indicating CDW-like distortions confined to the metal sublattice.

The analysis below focuses on $Sr_3B_8C_8H_8$ because its parent compound $Sr_2B_6C_6$ has been synthesized.[43] A key distinction between the 2D and 3D structures is the loss of chemical equivalence among the carbon and boron atoms in the clathrane. As a result, the conduction band states that are triply degenerate at the Γ point, located ∼1.5 eV above the Fermi level (E_F) in $Sr_2B_6C_6$,[43] split in the 2D structure, with a total energy separation of 1.5 eV (Figure 2A). Compared to the 3D system, the uppermost band shifts from E_F + 1.5 eV to E_F + 1.8 eV, while the remaining two (nondegenerate) states are stabilized and become nearly flat, lying ∼0.3 eV above E_F. To better understand the electronic structure of this clathrane, we calculated its partial charge densities within the chosen energy windows. The green region in Figure 2A, spanning an energy range of ±0.1 eV around E_F + 1 eV, cuts through the aforementioned dispersive band. Its computed charge density resembles π-type orbitals centered on unpassivated B/C atoms that point along the *a* lattice vector, encompassing the B_2C_2 square in the central region of the clathrane layer (Figure 2B) with minimal contributions from the surface atoms. The projected density of states (PDOS) in this energy range is similar to that of the 3D clathrates, where boron and carbon contribute comparably, and no contribution from hydrogen is evident.[45,48,49] Notably, the boron atoms that contribute significantly to the charge density in the green-shaded region do not contribute at all to the region shaded in blue. As a result, the PDOS near E_F contains significantly larger carbon character, a feature rarely observed in the 3D counterparts. Additionally, the hydrogen atoms, which passivate the structure, contribute modestly to the PDOS around E_F. This hydrogen character is evident in the charge density plot, especially the lower panel in Figure 2C. Another notable feature is the nearly flat electronic DOS, a hallmark of a 2D system, around E_F, contrasting the nearly parabolic DOS in $Sr_2B_6C_6$.

The three bands that cross E_F form the 2D Fermi surface of $Sr_3B_8C_8H_8$ (Figure 2D), and they can participate in the superconducting mechanism. The Fermi surface is characterized by nearly vertical features located at $k_x \approx 0.1$, which

https://doi.org/10.1021/acs.nanolett.5c04166
Nano Lett. 2025, 25, 15081−15088

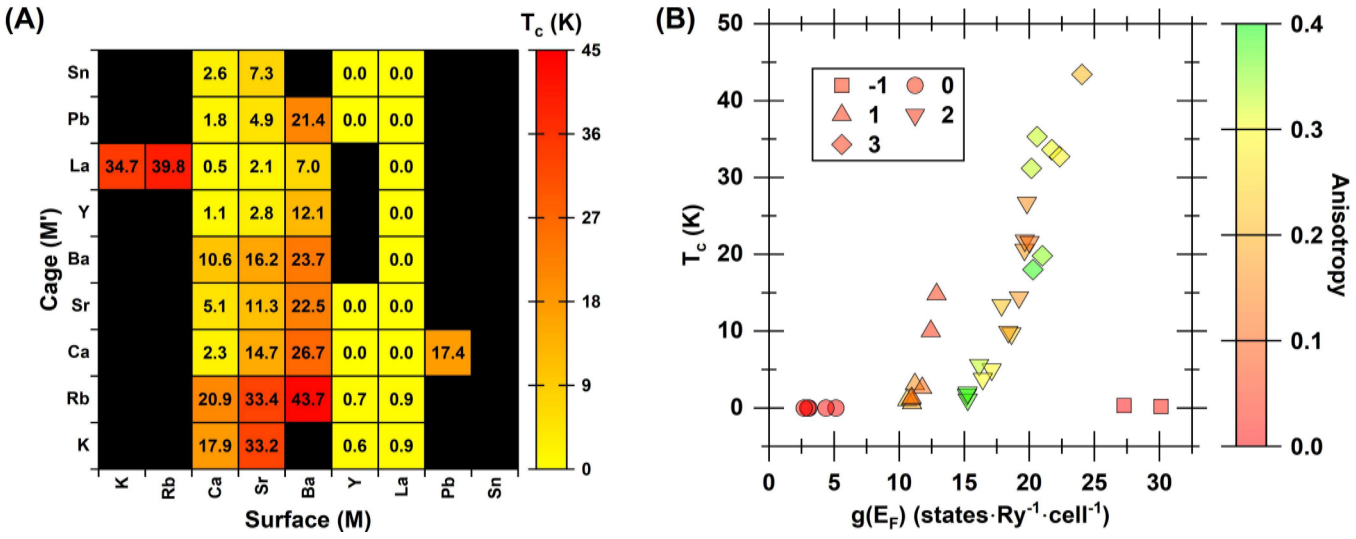

Figure 3. (a) Summary of the superconducting transition temperatures (T_c) for various $M_2M'B_8C_8H_8$ compositions under zero external stress, i.e., fully relaxed in-plane lattice constants. The T_c values are calculated using the Eliashberg theory with μ^* of 0.1; for systems with T_c < 10 K, values are estimated using the Allen−Dynes-modified McMillan formula, shown to be adequate for such high-throughput studies.[61] (b) Correlation between T_c, the DOS at the Fermi level, $g(E_F)$, and the in-plane structural anisotropy in angstroms (quantified by the lattice constant difference $b - a$). The inset shows the symbols employed for systems with the listed number of holes or with an excess electron (denoted by −1).

enable favorable Fermi surface nesting across a wide range of **q** vectors along the Γ−Y path. This nesting condition is clearly manifested in the phonon spectrum (Figure 2E), where three relatively flat phonon branches near 470, 530, and 630 cm^{-1} display strong electron-phonon coupling (EPC) along the Γ−Y direction, consistent with the three dominant peaks in the Eliashberg spectral function. Significant EPC-active modes are also found near the M point; the nesting vector **q** = (0.5, 0.5) connects sections of the Fermi surface (black arrow in Figure 2D), emphasizing the anisotropic nature of the EPC. Significant EPC is also found along the other high-symmetry lines in the Brillouin zone, although in a very narrow frequency range.

The dominant EPC mechanism in bulk SrB_3C_3 arises from the interaction between C 2p states and an E_g phonon mode near Γ, involving out-of-plane displacements of boron atoms, leading to distortions of the B_2C_2 squares.[45] We identified a similar vibrational mode in $Sr_3B_8C_8H_8$ at ∼640 cm^{-1}; however, it contributed significantly to EPC only near the zone center, and its contribution rapidly decayed moving away from Γ. Visualization of the three aforementioned phonon branches with large EPC in the clathrane reveals a Jahn−Teller-like distortion of the B_2C_2 units, transforming square motifs into rectangles. The 470 cm^{-1} mode corresponds to distortions of the central *ab*-plane square within the cage; the 630 cm^{-1} mode involves similar distortions at the surface *ab*-plane square but with additional motion from the hydrogen atoms increasing its frequency. The 530 cm^{-1} mode primarily involves distortions of the *ac*-plane square. Previously, we identified a similar Jahn−Teller mechanism as being a dominant contributor to the EPC in many $MM'B_6C_6$ systems with 2 or 3 holes per formula unit.[48] These compounds, such as $KPbB_6C_6$, typically exhibited phonon softening; however, such a softening is absent in $Sr_3B_8C_8H_8$. This combination of broken degeneracy in the electronic structure and the relatively "hard" phonon modes weakens the EPC in $Sr_3B_8C_8H_8$, resulting in a moderate coupling constant of λ = 0.55 (compared to λ = 0.92 in SrB_6C_6[45]). The high-frequency B−H and C−H stretches do not contribute significantly to EPC in $Sr_3B_8C_8H_8$. Nonetheless, a logarithmic average phonon frequency, ω_{log}, of 600 K is obtained, slightly higher than that of the bulk (544 K),[45] reflecting the lack of phonon softening. Solving the isotropic Eliashberg equations with μ^* = 0.1 yields a T_c value of 11.3 K, significantly lower than the theoretically predicted T_c of 40 K for bulk $Sr_2B_6C_6$.[45]

The T_c values of binary $MM'B_6C_6$ compounds correlate with the level of hole doping, with the highest values obtained for metals with an average charge of +1.5.[45,48−50] While the valence and radius of the metal atoms are important for the 2D clathranes, an additional distinguishing feature—also intimately linked to the hole doping and ionic size—is the in-plane structural anisotropy. This anisotropy arises from the inequivalent in-plane atomic configurations: carbon atoms align along the equatorial *a* axis, while boron atoms align along the *b* axis (Figure 1B). A similar anisotropy is present in 2D B_2O and hydrogenated β_{12}-borophene.[32,41] To capture this effect, we fully optimized the in-plane lattice parameters *a* and *b*, imposing zero stress along both directions. The resulting difference in lattice constants ($b - a$) serves as a metric for quantifying the degree of in-plane anisotropy. We find that structures with a higher hole concentration generally exhibit larger anisotropy (Figure S1). In compositions such as La_3, La_2Y, Y_2La, and Y_3, where all B/C 2p orbitals are fully occupied and any excess electrons reside in the metal d states, the lattice distortion is minimal, with anisotropy values typically below 0.1 Å. In contrast, 1 h^+ structures exhibit anisotropies ranging from 0.05 to 0.25 Å, 2 h^+ from 0.12 to 0.39 Å, and 3 h^+ from 0.21 to 0.52 Å. Among clathranes with the same hole concentration, those incorporating metals with smaller ionic radii exhibit larger anisotropy (Figure S1), indicating a synergistic effect between the doping level and cation size. Importantly, this anisotropy competes with superconductivity, suggesting a trade-off between lattice distortion and optimal EPC.

For 3D clathrates, the T_c values within a given hole-doping group are relatively consistent, ranging from 30 to 44 K for 1

https://doi.org/10.1021/acs.nanolett.5c04166
Nano Lett. 2025, 25, 15081−15088

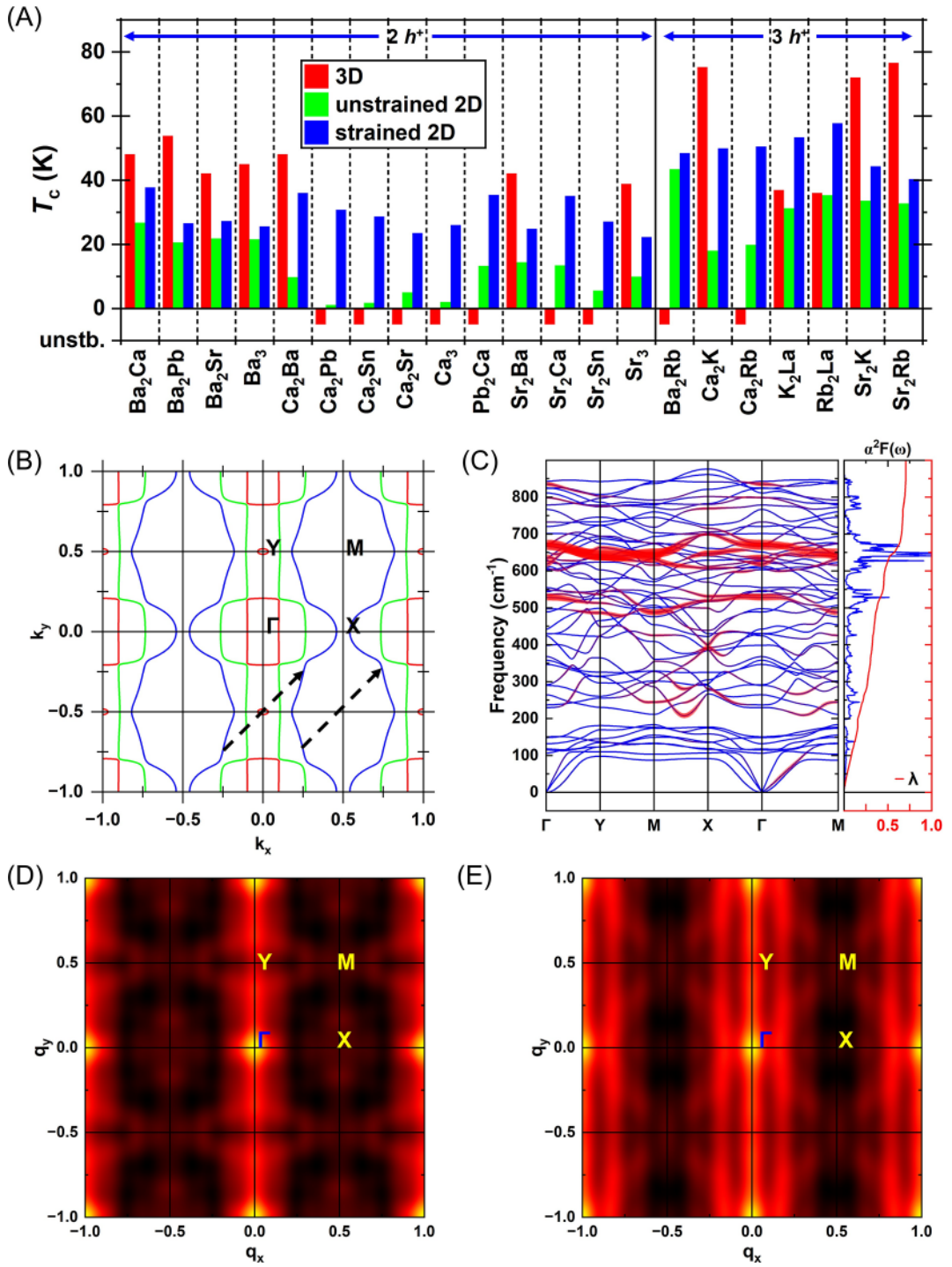

Figure 4. (a) Comparative summary of T_c in 3D bulk $MM'B_6C_6$, unstrained 2D $M_2M'B_8C_8H_8$, and biaxially strained 2D $M_2M'B_8C_8H_8$. The T_c values are calculated using Eliashberg theory with μ^* of 0.1; for systems with T_c < 10 K, values are estimated using the Allen−Dynes-modified McMillan formula. Ca_2Pb, Ca_2Sn, Ca_2Sr, Ca_3, Pb_2Ca, Sr_2Ca, Sr_2Sn, Ba_2Rb, and Ca_2Rb are dynamically unstable in 3D but stable in the 2D analogues. (b) Fermi surface of biaxially strained 2D $Sr_3B_8C_8H_8$. (c) Phonon dispersion, Eliashberg spectral function, $\alpha^2F(\omega)$, and the integrated electron−phonon coupling constant, $\lambda(\omega)$, within the frequency range of 0−900 cm^{-1}. The width of the red lines in the phonon dispersion corresponds to the mode-resolved electron−phonon coupling strength, proportional to $\lambda_{q\nu}\omega_{q\nu}$ for each phonon mode ν at wavevector $\mathbf{q}$. The plot in the full frequency range is available in the Supporting Information. (d) 2D nesting function, $\chi(\mathbf{q})$, of unstrained $Sr_3B_8C_8H_8$. (e) Nesting function of biaxially strained $Sr_3B_8C_8H_8$.

h^+ systems, from 40 to 54 K for 2 h^+, and from 72 to 88 K for 3 h^+.[48] In contrast, 2D clathranes show a broader and more irregular T_c spread (Figure 3A), suggesting that additional factors are at play. For example, within the 1 h^+ group, T_c ranges from 0 to 15 K, for 2 h^+, from 1 to 27 K, and for 3 h^+, from 18 to 43 K. Figure 3B illustrates T_c, in-plane anisotropy, and the electronic DOS at the Fermi level $[g(E_F)]$. In general, an increased number of holes leads to higher $g(E_F)$, consistent with enhanced metallicity. An exception is seen in electron-doped species (−1 hole, e.g., La_3, La_2Y, Y_2La, Y_3), which

https://doi.org/10.1021/acs.nanolett.5c04166
Nano Lett. 2025, 25, 15081−15088

exhibit the highest $g(E_F)$ from the metal d states. Because such d states may, in principle, call for a DFT+U treatment, magnetism could emerge if correlations are included; however, we do not expect T_c in such systems to be high based upon the values calculated for their nonmagnetic counterparts. Structures with zero holes are nominally semiconducting, although in some cases, band overlap results in a small but nonzero $g(E_F)$. Notably, structures with anomalously low T_c—despite having favorable doping levels—exhibit larger in-plane anisotropy compared to other members of the same group, reinforcing the conclusion that in-plane anisotropy suppresses superconductivity in 2D clathranes, disrupting the otherwise robust correlation between hole doping and T_c observed in their 3D counterparts.

While the relationship between anisotropy and superconductivity likely involves multiple intertwined effects, it is clear that larger in-plane anisotropy correlates with suppressed T_c. To determine if a physical approach mitigating the anisotropy by biaxial strain could enhance T_c, computations were performed that restored the in-plane lattice constants to those of the corresponding 3D clathrates by simultaneously elongating the a lattice vector and contracting the b lattice vector. We focused on the compositions with 2 h^+ and 3 h^+ because their T_c values were typically higher (Figure 3B). Comparing T_c values across the 3D clathrates, unstrained 2D clathranes, and biaxially strained clathranes revealed that the 3D phases generally exhibit the highest T_c, with exceptions such as K_2La and Rb_2La (Figure 4A). The degeneracy breaking in the 2D structures weakens the EPC, accounting for the lower T_c values in most cases. Conversely, some dynamically unstable 3D frameworks possess stable clathrane analogues—particularly those containing Ca and Sn. Biaxial strain enhances T_c relative to the fully optimized systems, with an average increase of 15.5 K (Figure 4A), e.g., the T_c of $Sr_3B_8C_8H_8$ increases from 11.3 to 22.2 K upon straining. This enhancement can be traced to subtle modifications in the electronic band structure: elongation of the a axis results in flatter bands along Γ−X and steeper bands along Y−M, shifting the Fermi crossing points closer to X and Y, respectively (Figure 4B), with concomitant changes in the EPC-active modes (Figure 4C). Strain enhances the nesting along the Γ−M direction, as evidenced by the 2D nesting functions (cf. Figure 4D and E). These improved nesting features activate the same EPC modes as those in the unstrained case but with stronger contributions extending from the Γ−Y direction to a broader range of $\mathbf{q}$ vectors along Γ−Y−M and Γ−M (Figure 4C), increasing λ from 0.55 to 0.71. However, this enhancement comes with a trade-off: low-frequency phonons around 200 cm^{-1} become EPC-active due to mode softening along Γ−M and M−X. These phonon modes involve out-of-plane displacements of boron atoms, following the E_g character described for 3D $Sr_2B_6C_6$[45] and decreasing ω_{log} from 600.3 to 531.4 K.

In conclusion, a family of 2D metal borocarbide clathranes, derived from 3D $MM'B_6C_6$ clathrate counterparts, some which have recently been synthesized,[42−44] were proposed. DFT calculations demonstrated that the dynamic and thermodynamic stability of the 2D analogues can be achieved via appropriate surface metal decoration and hydrogen passivation, yielding stable $M_2M'B_8C_8H_8$ compositions. The Fermi level and hole concentration can be tuned by varying the metal atoms, enabling metallicity and superconductivity. Unlike their 3D analogues, the 2D clathranes exhibit in-plane anisotropy, which competes with, and in some cases suppresses, superconductivity. Clathranes with high anisotropy typically show reduced EPC and lower T_c values, despite favorable doping levels, whereas biaxial strain reduces anisotropy and enhances the superconducting properties. Strain engineering increased T_c by an average of 15.5 K, with $Sr_3B_8C_8H_8$ exhibiting T_c enhancement from 11.3 to 22.2 K. This study establishes 2D clathranes as a promising platform for tunable superconductivity and highlights the interplay between hole doping, lattice anisotropy, and electron−phonon interactions.

■ ASSOCIATED CONTENT

Data Availability Statement

The data that support the findings of this study are openly available in the NOMAD Repository under DOI 10.17172/NOMAD/2025.09.15-1.

Supporting Information

The Supporting Information is available free of charge at https://pubs.acs.org/doi/10.1021/acs.nanolett.5c04166.

Full computational details, extra analysis on thermodynamics, projected phonon line widths and Eliashberg spectral functions, phonon band structures and DOS, electronic structure analysis, trajectories of molecular dynamics runs, and structural parameters (PDF)

■ AUTHOR INFORMATION

Corresponding Authors

Xiaoyu Wang − *Department of Chemistry, University at Buffalo, Buffalo, New York 14261, United States;* orcid.org/0000-0001-7549-6010; Email: xwang224@buffalo.edu

Eva Zurek − *Department of Chemistry, University at Buffalo, Buffalo, New York 14261, United States;* orcid.org/0000-0003-0738-867X; Email: ezurek@buffalo.edu

Authors

Warren E. Pickett − *Department of Physics and Astronomy, University of California—Davis, Davis, California 95616, United States*

Matthew N. Julian − *Intellectual Ventures, Bellevue, Washington 98007, United States*

Rohit P. Prasankumar − *Intellectual Ventures, Bellevue, Washington 98007, United States;* orcid.org/0000-0003-0902-2831

Complete contact information is available at: https://pubs.acs.org/10.1021/acs.nanolett.5c04166

Notes

The authors declare no competing financial interest.

■ ACKNOWLEDGMENTS

This work was supported by the Deep Science Fund of Intellectual Ventures and NSF Award DMR-2119065. Calculations were performed at the Center for Computational Research (http://hdl.handle.net/10477/79221) at SUNY Buffalo. We thank Timothy Strobel and Stu Wolf for fruitful discussions.

■ REFERENCES

(1) Lang, W. In *Encyclopedia of Condensed Matter Physics*, 2nd ed.; Chakraborty, T., Ed.; Academic Press: Oxford, U.K., 2024; pp 368−380.

(2) Krogstrup, P.; Ziino, N.; Chang, W.; Albrecht, S.; Madsen, M.; Johnson, E.; Nygård, J.; Marcus, C. M.; Jespersen, T. Epitaxy of semiconductor−superconductor nanowires. *Nat. Mater.* **2015**, *14*, 400−406.
(3) Ruf, J. P.; Paik, H.; Schreiber, N. J.; Nair, H. P.; Miao, L.; Kawasaki, J. K.; Nelson, J. N.; Faeth, B. D.; Lee, Y.; Goodge, B. H.; Pamuk, B.; Fennie, C. J.; Kourkoutis, L. F.; Schlom, D. G.; Shen, K. M. Strain-stabilized superconductivity. *Nat. Commun.* **2021**, *12*, 59.
(4) Shalnikov, A. Superconducting thin films. *Nature* **1938**, *142*, 74.
(5) Saito, Y.; Nojima, T.; Iwasa, Y. Highly crystalline 2D superconductors. *Nat. Rev. Mater.* **2017**, *2*, 16094.
(6) Zhang, T.; Cheng, P.; Li, W.-J.; Sun, Y.-J.; Wang, G.; Zhu, X.-G.; He, K.; Wang, L.; Ma, X.; Chen, X.; Wang, Y.; Liu, Y.; Lin, H.-Q.; Jia, J.-F.; Xue, Q.-K. Superconductivity in one-atomic-layer metal films grown on Si (111). *Nat. Phys.* **2010**, *6*, 104−108.
(7) Liu, X.; Hersam, M. C. 2D materials for quantum information science. *Nat. Rev. Mater.* **2019**, *4*, 669−684.
(8) Shabani, J.; Kjaergaard, M.; Suominen, H. J.; Kim, Y.; Nichele, F.; Pakrouski, K.; Stankevic, T.; Lutchyn, R. M.; Krogstrup, P.; Feidenhans'l, R.; Kraemer, S.; Nayak, C.; Troyer, M.; Marcus, C. M.; Palmstrøm, C. J. Two-dimensional epitaxial superconductor-semiconductor heterostructures: A platform for topological superconducting networks. *Phys. Rev. B* **2016**, *93*, 155402.
(9) Gupta, M.; Graziano, G. V.; Pendharkar, M.; Dong, J. T.; Dempsey, C. P.; Palmstrøm, C.; Pribiag, V. S. Gate-tunable superconducting diode effect in a three-terminal Josephson device. *Nat. Commun.* **2023**, *14*, 3078.
(10) Xue, M.; Chen, G.; Yang, H.; Zhu, Y.; Wang, D.; He, J.; Cao, T. Superconductivity in potassium-doped few-layer graphene. *J. Am. Chem. Soc.* **2012**, *134*, 6536−6539.
(11) Li, K.; Feng, X.; Zhang, W.; Ou, Y.; Chen, L.; He, K.; Wang, L.; Guo, L.; Liu, G.; Xue, Q.; Ma, X. Superconductivity in Ca-intercalated epitaxial graphene on silicon carbide. *Appl. Phys. Lett.* **2013**, *103*, 062601.
(12) Tiwari, A. P.; Shin, S.; Hwang, E.; Jung, S.-G.; Park, T.; Lee, H. Superconductivity at 7.4 K in few layer graphene by Li-intercalation. *J. Phys.: Conden. Matter* **2017**, *29*, 445701.
(13) Frindt, R. Superconductivity in ultrathin $NbSe_2$ layers. *Phys. Rev. Lett.* **1972**, *28*, 299.
(14) Ugeda, M. M.; Bradley, A. J.; Zhang, Y.; Onishi, S.; Chen, Y.; Ruan, W.; Ojeda-Aristizabal, C.; Ryu, H.; Edmonds, M. T.; Tsai, H.-Z.; Riss, A.; Mo, S.-K.; Lee, D.; Zettl, A.; Hussain, Z.; Shen, Z.-X.; Crommie, M. F. Characterization of collective ground states in single-layer $NbSe_2$. *Nat. Phys.* **2016**, *12*, 92−97.
(15) Tsen, A.; Hunt, B.; Kim, Y.; Yuan, Z.; Jia, S.; Cava, R.; Hone, J.; Kim, P.; Dean, C.; Pasupathy, A. Nature of the quantum metal in a two-dimensional crystalline superconductor. *Nat. Phys.* **2016**, *12*, 208−212.
(16) Xi, X.; Wang, Z.; Zhao, W.; Park, J.-H.; Law, K. T.; Berger, H.; Forró, L.; Shan, J.; Mak, K. F. Ising pairing in superconducting $NbSe_2$ atomic layers. *Nat. Phys.* **2016**, *12*, 139−143.
(17) Wang, Z.; Cheon, C.-Y.; Tripathi, M.; Marega, G. M.; Zhao, Y.; Ji, H. G.; Macha, M.; Radenovic, A.; Kis, A. Superconducting 2D NbS_2 grown epitaxially by chemical vapor deposition. *ACS Nano* **2021**, *15*, 18403−18410.
(18) Li, L.; O'farrell, E.; Loh, K.; Eda, G.; Özyilmaz, B.; Castro Neto, A. Controlling many-body states by the electric-field effect in a two-dimensional material. *Nature* **2016**, *529*, 185−189.
(19) Profeta, G.; Calandra, M.; Mauri, F. Phonon-mediated superconductivity in graphene by lithium deposition. *Nat. Phys.* **2012**, *8*, 131−134.
(20) Yang, Q.; Zhang, H.; Zhao, J.; Jiang, X. Probing the superconductivity limit of Li-doped graphene. *Adv. Funct. Mater.* **2024**, *34*, 2406023.
(21) Zheng, F.; Zhou, Z.; Liu, X.; Feng, J. First-principles study of charge and magnetic ordering in monolayer $NbSe_2$. *Phys. Rev. B* **2018**, *97*, 081101.
(22) Lian, C.-S.; Si, C.; Duan, W. Unveiling charge-density wave, superconductivity, and their competitive nature in two-dimensional $NbSe_2$. *Nano Lett.* **2018**, *18*, 2924−2929.
(23) Campi, D.; Kumari, S.; Marzari, N. Prediction of phonon-mediated superconductivity with high critical temperature in the two-dimensional topological semimetal W_2N_3. *Nano Lett.* **2021**, *21*, 3435−3442.
(24) Liu, P.-F.; Zheng, F.; Li, J.; Si, J.-G.; Wei, L.; Zhang, J.; Wang, B.-T. Two-gap superconductivity in a Janus MoSH monolayer. *Phys. Rev. B* **2022**, *105*, 245420.
(25) Ku, R.; Yan, L.; Si, J. G.; Zhu, S.; Wang, B. T.; Wei, Y.; Pang, K.; Li, W.; Zhou, L. Ab initio investigation of charge density wave and superconductivity in two-dimensional Janus 2H/1T-MoSH monolayers. *Phys. Rev. B* **2023**, *107*, 064508.
(26) Seeyangnok, J; Ul Hassan, M M; Pinsook, U; Ackland, G J Superconductivity and electron self-energy in tungsten-sulfur-hydride monolayer. *2D Mater.* **2024**, *11*, 025020.
(27) Seeyangnok, J.; Pinsook, U.; Ackland, G. J. Superconductivity and strain-enhanced phase stability of Janus tungsten chalcogenide hydride monolayers. *Phys. Rev. B* **2024**, *110*, 195408.
(28) Choi, H. J.; Roundy, D.; Sun, H.; Cohen, M. L.; Louie, S. G. The origin of the anomalous superconducting properties of MgB_2. *Nature* **2002**, *418*, 758−760.
(29) Bekaert, J.; Aperis, A.; Partoens, B.; Oppeneer, P. M.; Milošević, M. Evolution of multigap superconductivity in the atomically thin limit: Strain-enhanced three-gap superconductivity in monolayer MgB_2. *Phys. Rev. B* **2017**, *96*, 094510.
(30) Bekaert, J.; Petrov, M.; Aperis, A.; Oppeneer, P. M.; Milošević, M. Hydrogen-induced high-temperature superconductivity in two-dimensional materials: The example of hydrogenated monolayer MgB_2. *Phys. Rev. Lett.* **2019**, *123*, 077001.
(31) Dai, J.; Li, Z.; Yang, J.; Hou, J. A first-principles prediction of two-dimensional superconductivity in pristine B_2C single layers. *Nanoscale* **2012**, *4*, 3032−3035.
(32) Yan, L.; Liu, P.-F.; Li, H.; Tang, Y.; He, J.; Huang, X.; Wang, B.-T.; Zhou, L. Theoretical dissection of superconductivity in two-dimensional honeycomb borophene oxide B_2O crystal with a high stability. *npj Comput. Mater.* **2020**, *6*, 94.
(33) Li, H.; Han, F.; Wei, J.; Zhong, T.; Sun, J.; Zhang, Y.; Xu, M.; Li, Y.; Zhang, S. Emerging two-dimensional superconductors TiB_3C and $Ti_2B_3C_2$ with monolayer kagome borophene. *Appl. Surf. Sci.* **2025**, *686*, 162140.
(34) Modak, P.; Verma, A. K.; Mishra, A. K. Prediction of superconductivity at 70 K in a pristine monolayer of LiBC. *Phys. Rev. B* **2021**, *104*, 054504.
(35) Wines, D.; Choudhary, K.; Biacchi, A. J.; Garrity, K. F.; Tavazza, F. High-throughput DFT-based discovery of next generation two-dimensional (2D) superconductors. *Nano Lett.* **2023**, *23*, 969−978.
(36) Singh, S.; Romero, A. H.; Mella, J. D.; Eremeev, V.; Muñoz, E.; Alexandrova, A. N.; Rabe, K. M.; Vanderbilt, D.; Muñoz, F. High-temperature phonon-mediated superconductivity in monolayer $Mg_2B_4C_2$. *npj Quant. Mater.* **2022**, *7*, 37.
(37) da Silva, T. H.; Cavignac, T.; Cerqueira, T. F.; Wang, H.-C.; Marques, M. A. Machine-learning accelerated prediction of two-dimensional conventional superconductors. *Mater. Horiz.* **2025**, *12*, 3408−3419.
(38) Ou, M.; Wang, X.; Yu, L.; Liu, C.; Tao, W.; Ji, X.; Mei, L. The emergence and evolution of borophene. *Adv. Sci.* **2021**, *8*, 2001801.
(39) Penev, E. S.; Kutana, A.; Yakobson, B. I. Can two-dimensional boron superconduct? *Nano Lett.* **2016**, *16*, 2522−2526.
(40) Li, Q.; Kolluru, V. S. C.; Rahn, M. S.; Schwenker, E.; Li, S.; Hennig, R. G.; Darancet, P.; Chan, M. K.; Hersam, M. C. Synthesis of borophane polymorphs through hydrogenation of borophene. *Science* **2021**, *371*, 1143−1148.
(41) Soskic, B. N.; Bekaert, J.; Sevik, C.; Milosevic, M. V. Enhanced Superconductivity of Hydrogenated β12 Borophene. *Nano Lett.* **2024**, *24*, 12650−12657.

https://doi.org/10.1021/acs.nanolett.5c04166
Nano Lett. 2025, 25, 15081−15088

(42) Zhu, L.; Liu, H.; Somayazulu, M.; Meng, Y.; Gunka, P. A.; Shiell, T. B.; Kenney-Benson, C.; Chariton, S.; Prakapenka, V. B.; Yoon, H.; Horn, J. A.; Paglione, J.; Hoffmann, R.; Cohen, R. E.; Strobel, T. A. Superconductivity in SrB_3C_3 clathrate. *Phys. Rev. Res.* **2023**, *5*, 013012.
(43) Zhu, L.; Borstad, G. M.; Liu, H.; Gunka, P. A.; Guerette, M.; Dolyniuk, J.-A.; Meng, Y.; Greenberg, E.; Prakapenka, V. B.; Chaloux, B. L.; Epshteyn, A.; Cohen, R. E.; Strobel, T. A. Carbon-boron clathrates as a new class of sp3-bonded framework materials. *Sci. Adv.* **2020**, *6*, No. eaay8361.
(44) Strobel, T. A.; Zhu, L.; Guńka, P. A.; Borstad, G. M.; Guerette, M. A Lanthanum-Filled Carbon−Boron Clathrate. *Angew. Chem., Int. Ed.* **2021**, *133*, 2913−2917.
(45) Wang, J.; Yan, X.; Gao, M. High-temperature superconductivity in SrB_3C_3 and BaB_3C_3 predicted from first-principles anisotropic Migdal-Eliashberg theory. *Phys. Rev. B* **2021**, *103*, 144515.
(46) Zhang, P.; Li, X.; Yang, X.; Wang, H.; Yao, Y.; Liu, H. Path to high-T_c superconductivity via Rb substitution of guest metal atoms in the SrB_3C_3 clathrate. *Phys. Rev. B* **2022**, *105*, 094503.
(47) Gai, T.; Guo, P.; Yang, H.; Gao, Y.; Gao, M.; Lu, Z. Van Hove singularity induced phonon-mediated superconductivity above 77 K in hole-doped SrB_3C_3. *Phys. Rev. B* **2022**, *105*, 224514.
(48) Geng, N.; Hilleke, K. P.; Zhu, L.; Wang, X.; Strobel, T. A.; Zurek, E. Conventional high-temperature superconductivity in metallic, covalently bonded, binary-guest C−B clathrates. *J. Am. Chem. Soc.* **2023**, *145*, 1696−1706.
(49) Di Cataldo, S.; Qulaghasi, S.; Bachelet, G. B.; Boeri, L. High-Tc superconductivity in doped boron-carbon clathrates. *Phys. Rev. B* **2022**, *105*, 064516.
(50) Duan, Q.; Zhan, L.; Shen, J.; Zhong, X.; Lu, C. Predicting superconductivity near 70 K in 1166-type boron-carbon clathrates at ambient pressure. *Phys. Rev. B* **2024**, *109*, 054505.
(51) Sun, Y.; Zhu, L. Hydride units filled boron−carbon clathrate: a pathway for high-temperature superconductivity at ambient pressure. *Commun. Phys.* **2024**, *7*, 324.
(52) Zhao, W.; Sun, Y.; Li, J.; Yuan, P.; Iitaka, T.; Zhong, X.; Li, H.; Fang, Y.-W.; Liu, H.; Errea, I. Exploring the limits of superconductivity in metal-stuffed BC clathrates via ionic lattice anharmonicity. *arXiv* **2025**, arXiv:2501.12068.
(53) Zhu, S.; Yan, X.; Liu, J.; Oganov, A. R.; Zhu, Q. A revisited mechanism of the graphite-to-diamond transition at high temperature. *Matter* **2020**, *3*, 864−878.
(54) Xie, Y.; Zhang, X.; Liu, Z. Graphite to diamond: Origin for kinetics selectivity. *J. Am. Chem. Soc.* **2017**, *139*, 2545−2548.
(55) Khaliullin, R. Z.; Eshet, H.; Kühne, T. D.; Behler, J.; Parrinello, M. Nucleation mechanism for the direct graphite-to-diamond phase transition. *Nat. Mater.* **2011**, *10*, 693−697.
(56) Sorokin, P. B.; Yakobson, B. I. Two-dimensional diamond—diamane: Current state and further prospects. *Nano Lett.* **2021**, *21*, 5475−5484.
(57) Piazza, F.; Cruz, K.; Monthioux, M.; Puech, P.; Gerber, I. Raman evidence for the successful synthesis of diamane. *Carbon* **2020**, *169*, 129−133.
(58) Gregoryanz, E.; Ji, C.; Dalladay-Simpson, P.; Li, B.; Howie, R. T.; Mao, H.-K. Everything you always wanted to know about metallic hydrogen but were afraid to ask. *Matter Radiat. Extrem.* **2020**, *5*, 038101.
(59) Kvashnin, A. G.; Chernozatonskii, L. A.; Yakobson, B. I.; Sorokin, P. B. Phase diagram of quasi-two-dimensional carbon, from graphene to diamond. *Nano Lett.* **2014**, *14*, 676−681.
(60) Mortazavi, B.; Shojaei, F.; Javvaji, B.; Azizi, M.; Zhan, H.; Rabczuk, T.; Zhuang, X. First-principles investigation of mechanical, electronic and optical properties of H-, F-and Cl-diamane. *Appl. Surf. Sci.* **2020**, *528*, 147035.
(61) Pellegrini, C.; Sanna, A. Ab initio methods for superconductivity. *Nat. Rev. Phys.* **2024**, *6*, 509−523.

https://doi.org/10.1021/acs.nanolett.5c04166
Nano Lett. 2025, 25, 15081−15088